

Cite this: DOI: 10.1039/c1ee02279b

www.rsc.org/ees

PERSPECTIVE

Solution-processed colloidal quantum dot photovoltaics: A perspective

Ratan Debnath,^a Osman Bakr^{bc} and Edward H. Sargent^{*a}

Received 3rd August 2011, Accepted 15th September 2011

DOI: 10.1039/c1ee02279b

1. Introduction

Deployed solar cells today are predominantly first-generation devices based on silicon. Single-crystal materials offer the advantage of high efficiency, but costs associated with materials, manufacturing, and installation remain high. Second generation, or thin-film, technologies, such as those based on CdTe and CuInGaSe₂, offer dramatically improved costs per square meter, but at the price of lower efficiencies.

Third-generation photovoltaics aspire to unite high efficiency with low cost. Strategies include nanostructured semiconductors, inorganic–organic hybrid structures, and molecular assemblies.

Solution-processed colloidal quantum dot (CQD) photovoltaic devices offer considerable promise as a third-generation photovoltaic candidate. Their solution-synthesis and -coating offer a path to low-cost roll-to-roll manufacturing atop flexible, lightweight substrates. The bandgap of CQDs is tuned *via* the nanoparticles' diameter, allowing them to absorb the sun's broad visible and infrared spectrum within a single materials-processing strategy.

CQD photovoltaics have, with only a half-decade's intense activity, reached above 5% solar power conversion efficiency,^{1,2} and progress shows no signs of abating. Here we review the latest advances in the field and discuss the avenues for further progress towards commercially compelling performance. We include

a discussion of the materials themselves, considering their synthesis and their photophysical properties. We review briefly the fundamentals of semiconductors and solar cells. We highlight the major progress and achievements in CQD photovoltaics, focusing on the introduction of improved device architectures.

2. Fundamentals of solar cells

2.1 Materials engineering for broadband absorption

The sun's spectrum reaching the earth spans the visible and a considerable portion of the infrared. The solar spectrum, modified by atmospheric absorption and scattering, is standardized as the AM1.5G (air-mass 1.5 global) with an integrated power density of 100 W/m². Fig. 1 shows the AM1.5G spectrum juxtaposed with the bandgaps and absorbances of a variety of inorganic bulk semiconductors. Since the electrical power delivered consists of the product of current and voltage, and since selecting a larger bandgap can increase open-circuit voltage but diminish the absorbed photon current, an optimal bandgap lying in the range 1.1 and 1.4 eV is desired. This optimum is achieved using Si, CdTe, CdInSe₂, and quantum-confined PbS as familiar examples. Engineering tandem and multi-junction devices enables still more efficient use of the sun's spectrum.³

The absorption coefficient α , cm⁻¹ will determine the thickness of semiconductor material required for substantially complete light absorption. For an indirect bandgap semiconductor such as crystalline Si (c-Si), α is low ($\sim 10^2$ – 10^3 cm⁻¹) in significant portions of its absorbance spectrum, necessitating the use of \sim hundred-micrometer-thick films to absorb completely the incident solar flux above silicon's bandgap. Binary compound semiconductors such as CdTe and ternary/quaternary compounds such as CuInSe₂ and CuInGaSe₂ have the optimal

^aDepartment of Electrical and Computer Engineering, University of Toronto, 10 King's College Road, Toronto, Ontario, M5S 3G4, Canada. E-mail: ted.sargent@utoronto.ca

^bCenter for Solar and Alternative Energy Science and Engineering, King Abdullah University of Science and Technology (KAUST), Thuwal, 23955-6900, Saudi Arabia

^cPhysical Sciences and Engineering Division, King Abdullah University of Science and Technology (KAUST), Thuwal, 23955-6900, Saudi Arabia

Broader context

Continued growth in the worldwide demand for energy mandates investigation of technologies that improve the capture and storage of renewable sources. Solar energy is of intense interest, especially in light of its abundance. Solution-processed colloidal quantum dots (CQDs) offer an attractive route to low-cost, high-efficiency photovoltaics. The materials' prospects for low-cost derive from their convenient solution-phase synthesis and processing. Their potential for high efficiency comes from their wide spectral tunability, originating in the quantum size effect. Tunability enables systematic harvesting of photons from across the sun's broad spectrum. In this perspective, we highlight the recent progress in CQD based photovoltaics. We discuss prospects to enhance performance further *via* the development of new and improved materials and devices.

bandgaps combined with high α , leading to highly absorptive films only a few micrometers thick.

Tuning of bandgap *via* the quantum size effect opens up new candidate materials for solar photovoltaics. IV–VI semiconductors such as PbS and PbSe show strong confinement of electrons and holes, leading to dramatic increase in bandgap as nanoparticle size reaches below the ~ 20 nm Bohr exciton radius in these semiconductors.⁵

When the size of semiconductor becomes comparable to the natural length scale of the electron–hole pair, the quantum size effect becomes apparent as charge carriers' wavefunctions feel the boundaries of their container. The underlying discrete atomic orbitals possess energy labelled using atomic-like notations such as 1S, 1P, 1D, *etc.* as seen in Fig. 2.



Ratan Debnath

Ratan Debnath received his Dr.-Ing. from Technical University, Aachen, Germany PhD from University of Dundee, UK and Bachelor's degree from Indian Institute of Technology, Roorkee, India. He is currently working at National Institute of Standards and Technology (NIST) as a NIST-ARRA Senior Fellow. Previously, he worked as a e8/MITACS Post-doctoral Fellow at University of Toronto, Canada and a visiting scientist (DAAD-Helmholtz Fellow) at Research Center

Jülich, Germany. His research interests are in the synthesis and characterization of nanostructure materials with emphasis on energy applications.



Osman Bakr

Osman Bakr is an Assistant Professor of Materials Science and Engineering at King Abdullah University of Science & Technology (KAUST). He holds a B.Sc. in Materials Science and Engineering from MIT (2003) as well as a M.S. and Ph.D. in Applied Physics from Harvard University (2009). Bakr completed his doctoral training in the Supramolecular Nanomaterials Group of Francesco Stellacci at MIT. He then spent a year as a post-doctoral fellow in the Labora-

tory for Nanoscale Optics of Marko Loncar at Harvard University before joining KAUST as a faculty in 2010. Bakr's research interests include the synthesis, size-separation, and assembly of organic and organic-inorganic hybrid nanoparticles for solar cells, photonic and optoelectronic devices.

2.2 Photovoltaic device figures of merit

The canonical photovoltaic device is a p-n junction. At thermal equilibrium, no net current flows and the Fermi level is independent of position. The concentration gradient of holes and electrons produces a diffusion current that is balanced by a drift current arising from a depletion region formed at the junction. The *built-in-voltage* (V_{bi}) results from the electrostatic potential differences in the junction.

Schottky devices are one-sided versions of the p-n device. When a metal makes contact with a semiconductor, a Schottky barrier is formed at their interface that determines the current and capacitance in the solar cell (Fig. 3). The barrier height depends on the work function of the metal and the semiconductor properties. A built in potential across the junction forms the depletion region and is related to the metal work function, ϕ_m and the electron affinity of the semiconductor, ϕ_s . Schottky barrier devices suffer from high reverse saturation current density and the effects of Fermi level pinning at the metal-semiconductor junction.

Solar cells under illumination are modelled as diodes in parallel with a constant current source (Fig. 4). The source current I_L results from solar illumination. The current–voltage (I – V) characteristics (Fig. 5) are treated as the sum of dark and short-circuit photocurrent:

$$I = I_D - I_L = I_0 \left[\frac{qV}{ekT} - 1 \right] - I_L \quad (1)$$

where I_0 is the diode saturation current. When illuminated, the rectifying device's I – V is shifted to the fourth quadrant due to light-induced current generation. The current that flows in a solar cell when its contacts are shorted is known as *short-circuit current* (I_{sc}). When the dark current and photogenerated current cancel out each other (*i.e.* no external load is connected), the maximum potential that a solar cell can generate is known as *open-circuit voltage* (V_{oc}):

$$V_{oc} = \frac{kT}{q} \ln \left(\frac{I_{sc}}{I_0} + I_0 \right) \quad (2)$$



Edward H. Sargent

Ted Sargent is a Professor in Electrical and Computer Engineering at the University of Toronto where he holds the Canada Research Chair in Nanotechnology. He earned the B.Sc.Eng. (Engineering Physics) from Queen's University in 1995 and the PhD in Electrical and Computer Engineering from the University of Toronto in 1998. Since 1998 he has been on the faculty of the University of Toronto. In 2004–5 he was Visiting Professor at MIT. He is a Fellow of the AAAS and of the IEEE.

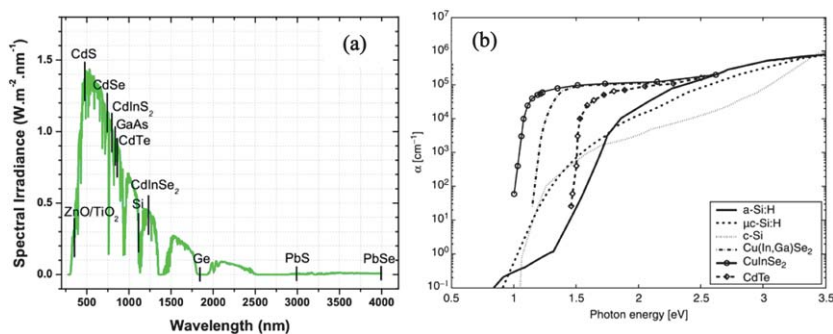


Fig. 1 (a) AM1.5G solar spectral irradiance of various bulk semiconductors employed in PV. (b) The optical absorption coefficient (α) vs. photon energy of various semiconductors that are used in solar cells.⁴

For ideal p-n junction solar cells, V_{oc} is equal to the difference in the quasi-Fermi level of electrons and holes in n-type and p-type material, respectively. For Schottky solar cells, it is the difference between the work function of the metal and the quasi-Fermi level of semiconductor.

A solar cell is operated in a regime from 0 to V_{oc} and it delivers the maximum power at voltage, V_m and current, I_m (Fig. 5). The quality or squareness of I - V curve defines the *fill-factor* (FF), the ratio of the maximum power under matched load to the product of V_{oc} and I_{sc} :

$$FF = \frac{I_m V_m}{I_{sc} V_{oc}} \quad (3)$$

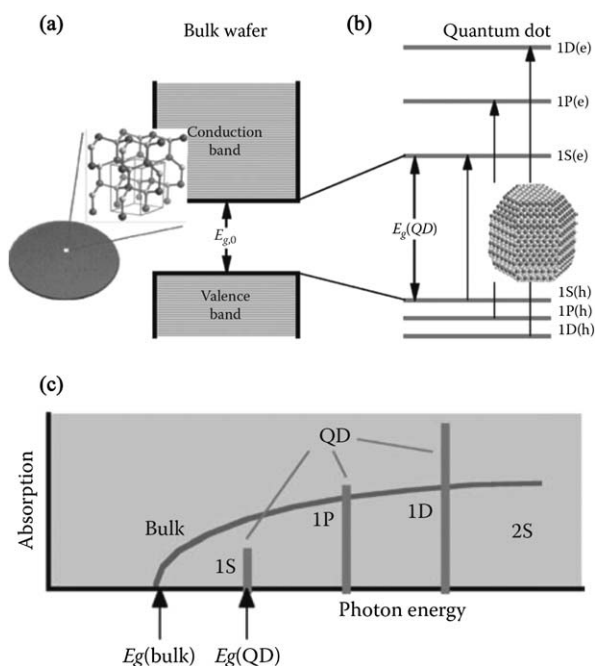


Fig. 2 (a) Energy bands of bulk semiconductor showing the continuity of conduction and valence band separated by a bandgap, E_g . (b) For QD, such continuity is broken and discrete atomic like states become available with energies determined by the size of the QD material. (c) Comparison of absorption spectra between a bulk semiconductor (curved line) and QD nanocrystal (vertical bars).⁶

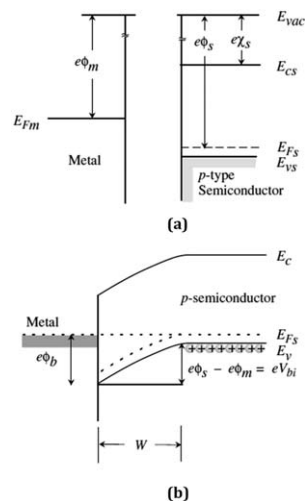


Fig. 3 A schematic of an ideal p-type Schottky barrier formation. (a) Individual energy levels of the metal and semiconductor. (b) Formation of a barrier when the metal makes contact with the semiconductor. Due to this built-in voltage (V_{bi}), a depletion region (W) is established.⁷

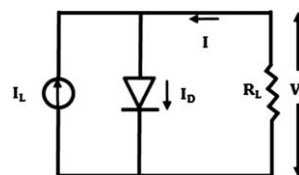


Fig. 4 Equivalent circuit of an ideal solar cell. I_0 is the diode saturation current whereas R_L is the load resistance.

Power conversion efficiency (η) of the cell is the ratio of electrical power generated by the cell (P_m) to the optical power (P_{in}) incident on the device:

$$\eta = \frac{P_m}{P_{in}} = \frac{I_{sc} V_{oc} FF}{P_{in}} \quad (4)$$

These four parameters (V_{oc} , I_{sc} , FF and η) are key figures of merit for a solar cell. In addition, external quantum efficiency (EQE) is the number of electrons flowing per second under short circuit condition ratioed to the rate of photons incident per

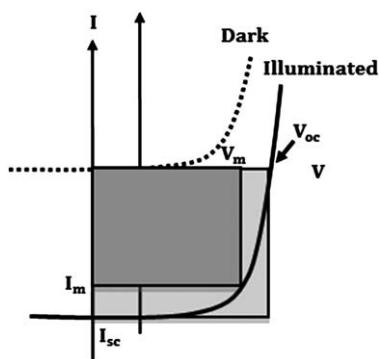


Fig. 5 The current–voltage curve of an ideal solar cell in the dark and illumination. Power density reaches maximum at a bias V_m shown by the inner rectangle.

second. Internal quantum efficiency (IQE) accounts instead for the rate of photons *absorbed* by the cell.

3. CQD materials: Synthesis, processing, and properties

3.1 Synthesis

Solution-phase synthesis begins with metal–organic precursors in coordinating solvents. Particle growth occurs *via* spontaneous nucleation and growth in a homogeneous solution of precursors and organic surfactants (Fig. 6). These surfactant molecules (*e.g.* various carboxylic, phosphonic acids, thiols, phosphines *etc.*) influence the kinetics of nucleation and growth of CQDs. When final precursor is injected into the coordinating solvents, thermal decomposition of the reagents takes place, and the precursor concentration is raised above the nucleation threshold. Rapid nucleation relieves this supersaturation. With the precursor concentration below the critical concentration for nucleation, no new nuclei are formed, and growth proceeds homogeneously across the solution. Further reduction of the concentration leads to Oswald ripening, wherein larger particles grow at an expense

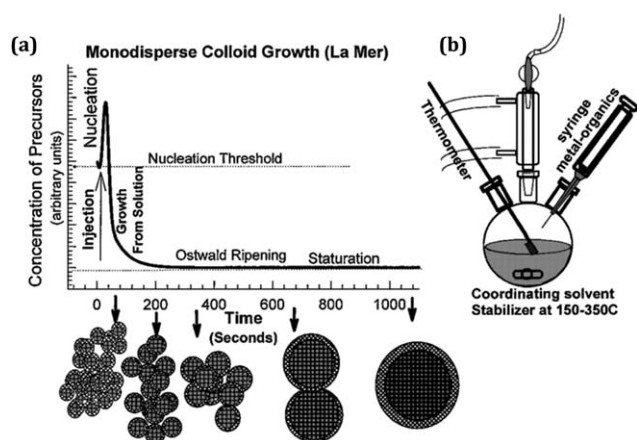


Fig. 6 (a) Schematics showing the nucleation and growth of colloidal nanocrystals in which a various sizes of crystals can be isolated at different time. (b) Simple synthetic apparatus showing the preparation of CQDs.⁸

of small ones. Longer reaction time yields larger particles, as does higher growth temperature.

Lead chalcogenide CQDs (*e.g.* PbS,⁹ PbSe¹⁰) and their alloys^{11,12} are of interest in photovoltaics by virtue of their small bulk bandgap and large potential for quantum confinement. Among these materials, PbS shows the greater stability in air.^{13,14} Various organic synthesis routes have been implemented to achieve highly monodispersed PbS nanocrystals. Typically, lead oleate precursor along with bis(trimethylsilyl)sulfide in octadecene produced 2.6–7.2 nm size range that corresponds to an absorption peak of 825–1750 nm.⁹ Syntheses instead employing lead chloride and sulphur along with oleylamine have also shown excellent size tunable and stable PbS CQDs. Very recently, excellent air stability have been demonstrated while using tri-n-octylphosphine during the synthesis and the average sizes between 3–10 nm had been achieved as shown in Fig. 7.¹⁵ Similarly, quantum confined PbSe CQD have also been synthesized using various synthetic routes with efficient, particle size tunable narrow bandwidth photoluminescence in mid-infrared.¹⁶

Designing nanocrystal core-shell structures of various compositions^{17–19} and dimensionalities^{20–23} adds a further element to quantum dot tuning: control over the spatial distribution of electrons and holes, and their interaction energies, within the CQD.²⁴

3.2 Doping

Doping nanocrystals enables further tuning of their optical and electronic properties.²⁵ Nanocrystals are a challenge to dope, since the crystal is prone to expel the dopants to its surface, a process known as self-purification.²⁵ Several doping strategies have been advanced in recent years including surface doping by treating the CQDs with particular ligands,^{26–28} introduction of the impurity ion during the nanocrystal growth reaction,²⁹ charge-transfer doping by binary co-assembly^{30,31} of donor/acceptor nanocrystals or core-shell³² structures.

A particularly promising route introduces impurity ions into preformed nanocrystals in solution, recently demonstrated by Mocatta *et al.*³³ in InAs at room temperature. Experiment and theory suggest controlled introduction of Ag (p-type) and Cu (n-type) impurities through solid-state diffusion, resulting in fine control over the Fermi energy *via* doping.³³ Doping preformed nanocrystals is attractive for its adaption of existing synthesis

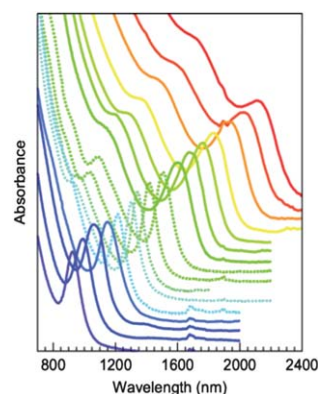


Fig. 7 Size dependent absorption spectra of PbS CQDs.¹⁵

protocols for narrowly-size-distributed nanocrystals with fewer modifications.

3.3 Superlattices

Superlattices³⁴ - quantum dot films exhibiting long-range order - offer superior charge transport properties compared to their spin-coated short-range ordered analogues.²⁴ Moreover, complex superlattices³⁵ composed of multiple types of ordered CQDs can exhibit novel properties not found in the original constituent CQDs.²⁴ For example, a 1 : 1 binary super-lattice of PbTe:Ag₂Te nanocrystals exhibits p-type doping of the PbTe phase by the Ag₂Te phase, and a two-order of magnitude increased conductivity compared to films comprised of pure PbTe or Ag₂Te.^{30,31}

The ligand-shell plays an important role in determining the distance between the nanocrystals, the transport properties,^{5,36} and superlattice symmetry in films.^{14,36-38} Optimal ligands for the synthesis of semiconductor CQDs are long and dynamically (*i.e.* weakly) passivate the surface of nanocrystals.²⁴ On the other hand, ligands that are best for device performance are short in order to promote inter-particle coupling, and are strongly bound to the nanocrystals surface to passivate mid-gap defect states. In order to obtain the desired electronic properties in CQD films, the post-synthesis ligands are frequently replaced with strongly-bound shorter ligands.^{26,39-41}

A new class of ligands, molecular metal chalcogenide complexes (MCCs), have recently attracted intense interest.⁴⁰ Organic ligands are replaced by negatively-charged inorganic MCCs such as SnS₄⁴⁻, Sn₂S₆⁴⁻, SnTe₄⁴⁻, AsS₃³⁻, MoS₄²⁻, and In₂Se₄²⁻.^{42,43} Spin-cast films of MCC-capped QDs benefit from dramatically higher reported mobilities than do their organic counterparts.^{42,43} The latest reports include measured electron mobilities as high as 16 cm² V⁻¹ s⁻¹, orders of magnitude higher than the best reported based on organic ligands.⁴² The improved performance was credited to the small size of MCCs and the appropriate energies of their HOMO and LUMO, which enhance the interparticle electronic coupling.⁴²

4. CQD photovoltaic devices

CQD solar cell efficiency has seen rapid progress in recent years since the first reports of optimal-single-junction-bandgap devices in 2005.⁴⁴ Various architectures have been realized with different types of CQD nanomaterials including Schottky (metal-CQD), heterojunction (Oxide-CQD), quantum dot sensitized solar cells,⁴⁵⁻⁴⁹ and hybrid structures,⁵⁰⁻⁵² as well as recent reports of tandem CQD photovoltaics. Heterojunction devices hold the record CQD solar efficiency to date 5.6%.²

4.1 Schottky

In CQD Schottky devices, a junction is formed between a p-type CQD solid and a shallow work function metal (Al, Mg, *etc.*). The mismatch in Fermi levels results in band bending at the interface. Electrons in the valence band are promoted, through light absorption, to the conduction band, leaving photoholes in the valence band. The resultant electron-hole pair is separated by the action of the electric field, electrons moving to the metal contact and holes to the ohmic contact.

For efficient operation, charge carrier extraction should outpace recombination, requiring the mobility to exceed $\tau V_{bi}/d$, where τ is the carrier life time, V_{bi} is the built-in-voltage, and d is the film thickness. While diffusion as well as drift has been characterized in these systems,⁵³ it is generally the case today that minority carrier diffusion proceeds inefficiently: the diffusion length of minority carriers is sufficiently small (*e.g.* typically tens of nm) in typical CQD films that extraction from the ~ 100 nm thick depletion region dominates the short-circuit current density. These facts combined lead to an absorption-extraction compromise, wherein thickening the absorber for complete absorption leads to a loss in internal quantum efficiency. Thus improving transport and recombination alike remains a crucial challenge for the field.

Most reported Schottky solar cells have employed lead-chalcogenide materials,^{14,26,41,54-58} with a few notable exceptions.⁵⁹⁻⁶¹ The first PbS CQD solar cells to exceed 1% AM1.5 efficiency are depicted in Fig. 8.²⁶ To improve charge transport within the nanocrystals film, long oleate ligands were replaced by much shorter *n*-butylamine ligand (~ 0.6 nm) *via* a solution-phase ligand exchange that preserved the colloidal stability of the nanocrystals. The device showed AM1.5G efficiency of 1.8% with a J_{sc} of 12.3 mA/cm², V_{oc} of 0.33 V and FF of 44%. For this device, the drift length for minority electrons was found to be 1 μ m, indicative of highly efficient extraction from within the depletion region.

The use of bidentate ligands, often introduced to render non-redispersible already-deposited colloidal quantum dot films, was reported in 2008.²⁷ Stability and performance alike were enhanced by the move to the strongly-bound bidentate ligand, 1,4-benzenedithiol (1,4-BDT), passivating PbSe.⁴¹ Electron and hole mobilities were improved relative to prior reports, with the benzene ring hypothesized to play a role in aiding carrier delocalization within the organic matrix. Nevertheless, similar efficiencies were subsequently reported using ethanedithiol shown in Fig. 9.⁵⁷

Recently, semiconductor/metal interfaces have been engineered to extend the device lifetime when operated in air and under continuous illumination.¹⁴ Prior to this advance, devices employing Al as Schottky contact degraded almost instantly due to oxidation at CQD film-metal interface. Introducing ~ 1 nm LiF atop Al decreased the oxidation process and dramatically improved device lifetime (Fig. 10).

CQD Schottky devices have been realized using ternary PbS_xSe_{1-x} CQDs synthesized using a one-pot, hot injection reaction.¹¹ S and Se anions were proven to be distributed uniformly in alloyed CQDs. The best choice of nanoparticle size and stoichiometry of S and Se led to 3.3% AM1.5 efficiency (Fig. 11).

Pre-encapsulation of PbS CQDs by dithio-carbamate ligands in combination with solid state treatment using thiols produced the Schottky CQD record of 3.6% in 2010.⁵⁶ The strongly-bound bidentate ligand 2,4,6-trimethyl-N-phenyl-N'-methyl-dithiocarbamate (TMPMDTC) passivated PbS CQDs as a result of a solution-phase exchange process. It also reduced the sensitivity of the materials to air ambient (Fig. 12) during processing. The low charge carrier density in these films increased the depletion region width to ~ 220 nm, a 50% increase compared to *n*-butylamine-PbS devices. The devices showed V_{oc} of 0.51V, J_{sc} of 14 mA/cm² and FF of 51%.

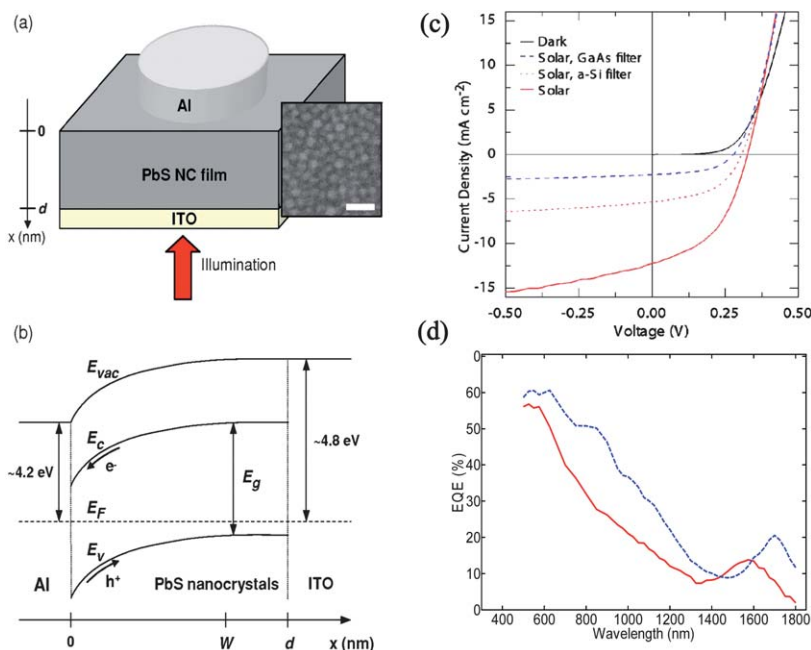


Fig. 8 (a) Schematic of the Schottky device architecture consisted of PbS CQDs as active material and Al as metal contact. The inset shows the electron micrograph of PbS film after n-butylamine exchange. (b) Energy band diagram showing the band bending takes place at Al/PbS interface. Under illumination, electrons and holes are swept away by the built-in electric field in the depletion layer. (c) Current–voltage data of the device influenced by the variation of the simulated solar illumination source. The device shows AM1.5 PCE of 1.8%. (d) EQE spectra for devices using PbS QDs having different excitonic peak.²⁶

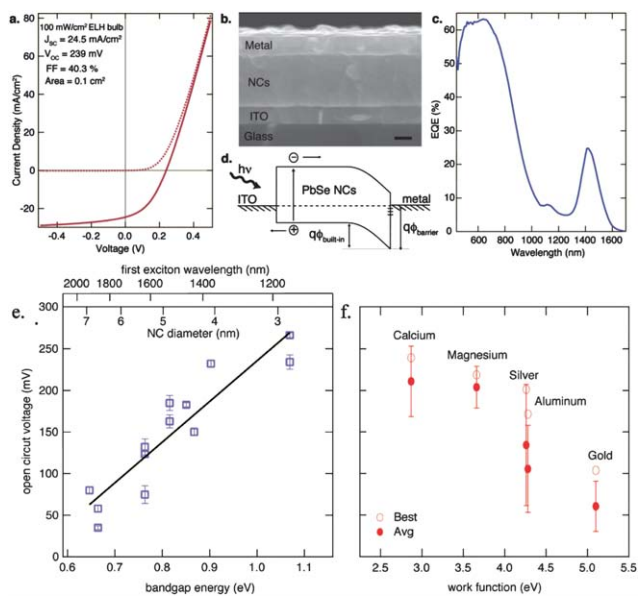


Fig. 9 (a) Current–voltage characteristics of EDT-PbSe device with high J_{sc} . (b) Electron micrograph of the device showing various components. (c) EQE plot yields above 60% in the visible. (d) Proposed equilibrium band diagram showing the separation of electrons and holes due to the built-in voltage. (e) Change of V_{oc} as a function of QD size *i.e.* V_{oc} increases when the QD size decrease using the same work function metal. (f) V_{oc} dependence for different metal work function using the same size of QD.⁵⁷

4.2 Depleted-heterojunction CQD photovoltaics

Schottky devices led the early years of CQD PV device advances. They suffer nonetheless some limitations. As the devices are

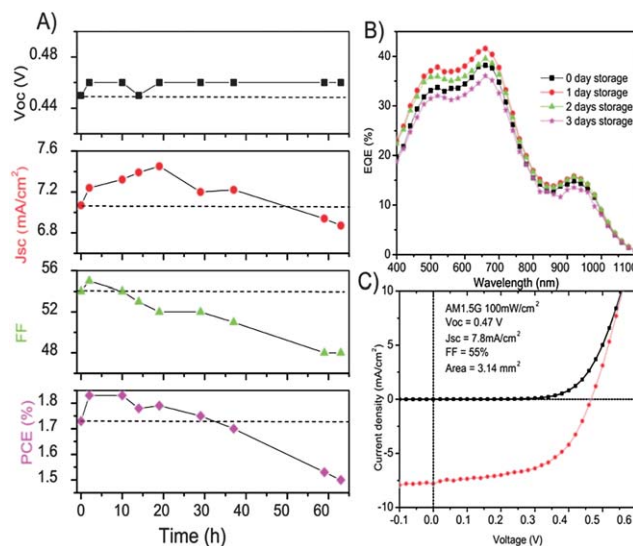


Fig. 10 Stability and performance of unpackaged Schottky device with ITO/PbS/LiF/Al/Ag. A) Device performance measured in air under simultaneous and continuous I - V scanning and simulated $100\text{mW}/\text{cm}^2$ AM1.5G illumination. B) Temporal evolution of EQE spectra of devices stored in air; C) Representative device performance in the dark and illumination.¹⁴

illuminated through the transparent ohmic contact, minority carriers generated on the side of illumination must travel through the entire thickness of the film before being collected by Schottky contact. These carriers are susceptible to recombination in view of the limited minority carrier diffusion in CQD films. V_{oc} is limited by Fermi-level pinning at semiconductor-metal interface

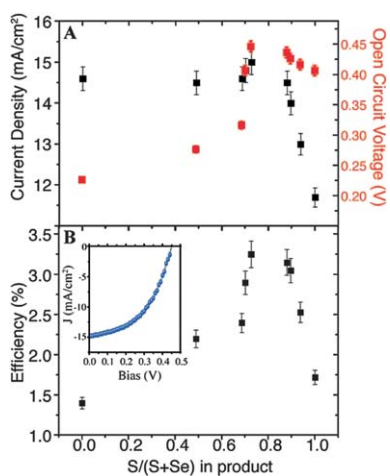


Fig. 11 (a) J_{sc}/V_{oc} and (b) efficiency characteristics of PbS_xSe_{1-x} Schottky device with different S concentration. The best efficiency was achieved for $PbS_{0.7}Se_{0.3}$ CQDs with $J_{sc} \sim 15 \text{ mA/cm}^2$ (inset).¹¹

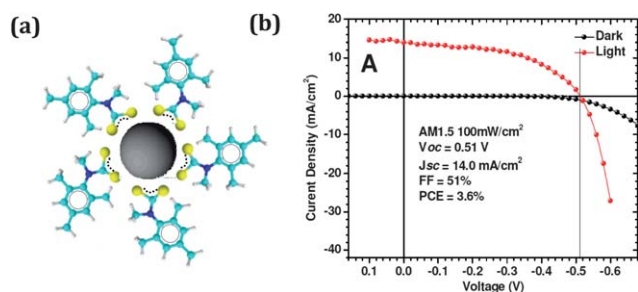


Fig. 12 (a) TMPMDTC ligand (yellow, sulfur; blue, nitrogen; cyan, carbon and white, hydrogen). (b) I - V characteristic TMPMDTC-PbS CQDs Schottky device.⁵⁶

due to the defect states. Back-recombination is a concern at the electron-extracting electrode due to the small barrier to hole injection.

Depleted-heterojunction (DH) CQD devices¹ overcome these above limitations by instead forming a junction between an n-type transparent electrode and a p-type CQD film. A type-II heterojunction may be engineered to provide an additional driving force for electron extraction while blocking holes at the junction.

The improvements were combined to produce a depleted heterojunction CQD device having greater than 5% solar power conversion efficiency.¹ The devices employed infrared-bandgap size-tuned PbS CQDs. TiO_2 acted as a transparent n-type electrode (Fig. 13). For PbS of diameter 3.7 nm, the 1S electron excited state of the CQD lies well above ($>0.3 \text{ eV}$) the TiO_2 conduction band level, and photo-excited electron injection into TiO_2 is therefore energetically favourable.

The 1P hole level sees a large ($>1.5 \text{ eV}$) discontinuity with the TiO_2 valence band, establishing a large barrier to the undesired passage of majority holes from the p-type CQD layer into the TiO_2 . The optimized DH architecture achieved FF over 60%, V_{oc} of 0.57 V and J_{sc} of $\sim 15 \text{ mA/cm}^2$ to reach 5.2% AM1.5G efficiency. EQE of these devices reached over 60% at short wavelengths and $\sim 24\%$ at the excitonic peak. Mott-Schottky analysis of capacitance-voltage behaviour indicated a free carrier density in PbS CQD film of $\sim 2 \times 10^{16} \text{ cm}^{-3}$. Depletion capacitance persisted up to a bias of 0.6 V - similar in magnitude to V_{oc} - consistent with the picture of a built-in-voltage separating photogenerated charge carriers.

A further advance in air-stability of CQD devices was reported in 2010.⁶² A CQD film was deposited on transparent ZnO nanocrystals electrodes *via* dip-coating method using 1,2-EDT as capping ligand. Light I - V data of the device using the X25 solar

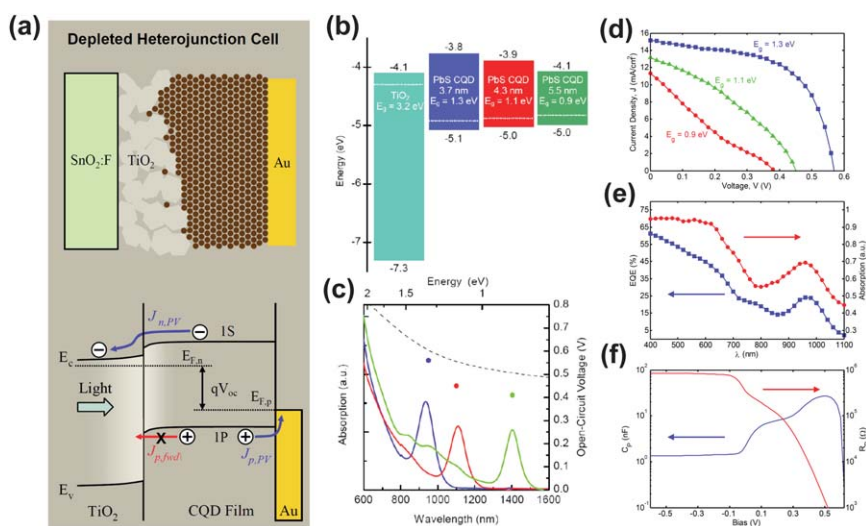


Fig. 13 (a) The DH architecture showing the various components of the device (FTO/porous TiO_2 /PbS QD/Au) along with the band diagram close to maximum V_{oc} . $E_{F,n}$ and $E_{F,p}$ are the electron and hole quasi-Fermi levels; E_c and E_v are the conduction and valence band edges; $J_{p,PV}$ and $J_{n,PV}$ are the hole and electron photocurrents (and are equal at steady-state); $J_{p, fwd}$ is the hole current in the forward bias direction. (b) Energy level alignment of TiO_2 and PbS CQD (1S, the first electronic excited state; 1P, the first excited hole state) of different sizes. The Fermi level is shown as a dashed line. (c) Solution absorption spectra in toluene of the three different PbS CQD sizes used in the device. (d) Current density- Voltage (J - V) response of photovoltaic devices from different CQD sizes. (e) EQE and absorption spectra of the best device with 1.3 eV bandgap. (f) Capacitance-voltage (C - V) curve of the DH device along with equivalent parallel resistance.¹

simulator under standard test conditions showed an overall efficiency of 2.94% with V_{oc} of 0.59 V and J_{sc} of 8.9 mA/cm². With 1000 h of light soaking, the device experienced essentially no loss in performance (Fig. 14).

The electron-acceptor in DH CQD solar cells have recently seen careful investigation and optimization.² By doping sol-gel derived TiO₂ with Zr, the band structure of the electrode was engineered to preserve, but minimize, the band offset between TiO₂ and optimal-single-junction-bandgap CQD PbS film. This resulted in good charge separation at the PbS/TiO₂ interfaces while minimizing any loss of open-circuit voltage. The resultant solar cell yielded a highest-reported CQD PV device efficiency of 5.6% (Fig. 15).

Further developments have also been taken place for engineering the metal ohmic contact. Gold has been replaced with lower-cost materials.⁶³ Using LiF-Ni as the top electrode led to similar performance to the case of Au (Fig. 16a). The insertion of the very thin LiF layer between PbS and Ni suppressed the interfacial reaction that was responsible for poor device performance. Transition metal oxides such as molybdenum oxide (MoO_x) also provide ohmic contacts, particularly when large-bandgap small-diameter PbS CQDs are employed (Fig. 16b). MoO_x is particularly a good alternative to Au as its work function is much deeper than Au, hence this can be used as an ohmic top contact for a wide range of PbS CQD sizes. Devices show performance similar to LiF/Ni and Au. Careful management of the top ohmic contact is important – otherwise, a substantial “dead zone” between PbS and the contact can limit carrier extraction.⁶⁴

4.3 Bulk heterojunction

The poor minority carrier diffusion length in existing CQD materials limits present-day device efficiencies. Improved

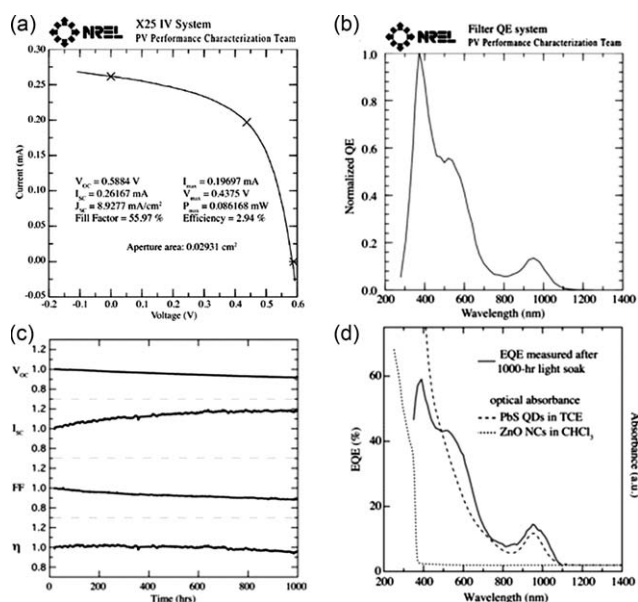


Fig. 14 (a) Measured I - V response of ZnO/PbS heterojunction device. (b) Normalized EQE of the same. (c) Device performance under constant illumination for 1000 h measured in air. (d) EQE spectrum of the device after the 1000-hour air stability assessment. Also, the optical absorption spectra of ZnO in chloroform and PbS in tetrachloroethylene are also shown.⁶²

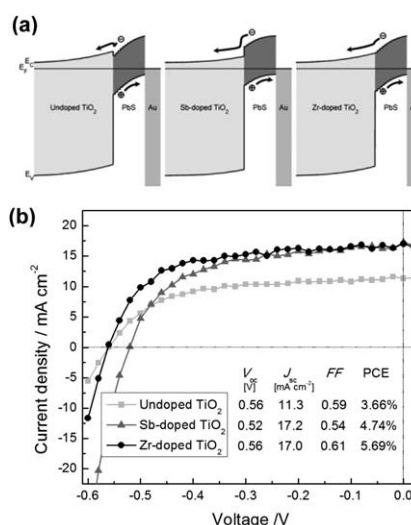


Fig. 15 (a) Schematic band diagram of the DH-CQD devices at equilibrium using various metal doped TiO₂. Zr-TiO₂ shows the optimal band alignment that combines maximal charge separation with high V_{oc} . (b) J - V characteristics of devices with different TiO₂ electrodes under simulated solar light.²

transport in CQD films will provide one notable solution. Device structure engineering provides another parallel avenue. Analogous to the bulk heterojunctions employed for the same reason in organic PV,⁶⁵ depleted bulk heterojunction (DBH) CQD devices⁶⁶ overcome the absorption-extraction compromise by using a nanostructured architecture.

The highest-performing of these devices led to solution-processed depleted bulk heterojunction (DBH) solar cells having AM1.5G efficiency of 5.5%.⁶⁶ They exhibited EQE greater than 40% at their excitonic peak. The devices used nanoporous TiO₂ in filtrated with PbS CQDs. The DBH architecture shown in Fig. 17 exploits highly porous electron accepting material having a pore radius slightly less than depletion width of the planar DH device. By modifying the band structure of TiO₂ electrode, the desirable band offset was achieved, suppressing bimolecular recombination. Across the near infrared and into the short-wavelength infrared, the DBH achieved substantially higher optical absorption (Fig. 17b), as intended. At exciton peak, the absorption was almost two-fold higher for the DBH device compared to the planar DH. The increased IR absorption of the DBH device results in a potential photocurrent enhancement of $\sim 30\%$, which was realized in a record J_{sc} of 20.6 mA/cm².

4.4 Multijunction CQD photovoltaics

The capacity to tune the bandgap of colloidal quantum dots (CQDs) has allowed the realization of optimal-bandgap single-junction solar cells discussed above. In principle it also allows tandem and multi-junction cells to be realized, devices that raise the ultimate limit on solar cell performance from 31% to 42% (tandem) and 49% (triple-junction).

Tandem CQD solar cells were recently reported in the PbS CQD materials system.⁶⁷ It was found that the engineering of a new, and efficient, recombination layer was required, that would be tailored to the requirements of CQD photovoltaics.

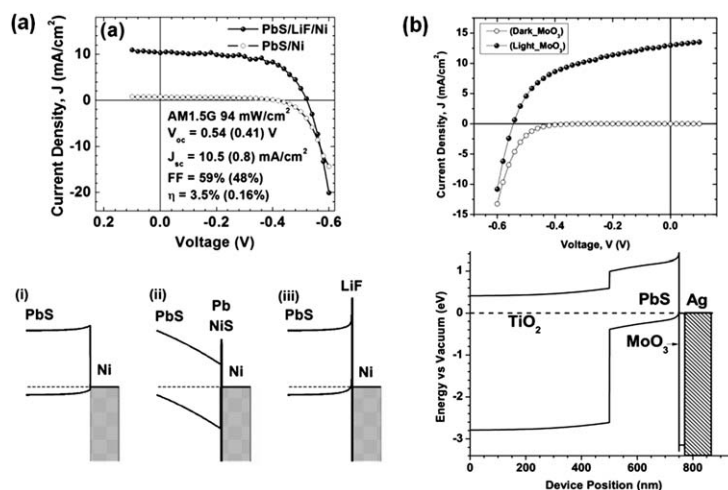


Fig. 16 (a) J-V response of devices made with and without LiF between PbS and Ni (top) along with the spatial band diagram at equilibrium (bottom) of (i) PbS–Ni while assuming no interfacial reaction *i.e.* sulphur interdiffusion, (ii) PbS–Pb/NiS–Ni, when sulphur interdiffusion takes place, and (iii) PbS–LiF–Ni when LiF acts as a thin tunnelling barrier and suppresses sulphur diffusion.⁶³ (b) J-V response from the device using MoO_x(10nm)/Ag(90nm) as top electrodes in dark and light (top). Spatial band diagram of DH-CQD cells at equilibrium employing MoO_x/Ag (bottom). MoO_x provides the required ohmic contact with PbS as well as back surface field.

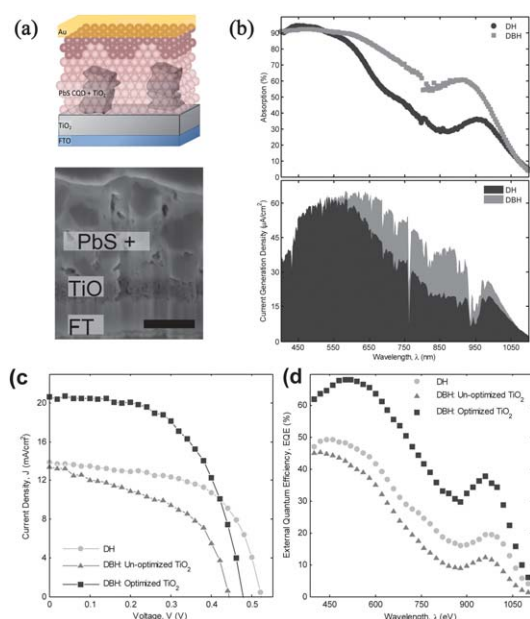


Fig. 17 (a) Schematic of the DBH devices (top) and SEM cross-section (bottom) showing infiltrated PbS CQD in TiO₂. (b) Single pass absorption spectra of the DH and DBH devices for comparison (top) and expected spectral photocurrent high shows 30% increase for DBH architecture (bottom). (c) J-V characteristics under AM1.5 simulated solar illumination for DH, un-optimized DBH and optimized DBH devices. (d) EQE spectra for same.⁶⁶

The device achieved current-matching of two monolithically-stacked depleted-heterojunction CQD solar cells. It employed colloidal quantum dots having exciton peaks at 1.6 eV for the visible junction (front cell) and 1 eV for the infrared junction (back cell).

The new recombination layer concept - termed graded recombination layer, or GRL - was implemented using

a progression of n-type transparent oxides that are readily available and CQD-compatible. The GRL progressed from deep-work-function n-type MoO₃ through intermediate indium tin oxide (ITO) to shallow-work-function but still heavily doped aluminium-doped zinc-oxide (AZO), the work function of which matches that of the lightly doped TiO₂ acceptor (Fig. 18). All materials are deposited using room-temperature sputtering processing.

The single-junction visible device (with transparent top contact) showed an open-circuit voltage (V_{oc1}) of 0.7 V and the single-junction IR device exhibited an open-circuit voltage (V_{oc2}) of 0.39 V. The ideal tandem cell should exhibit a V_{oc} equal to the sum of the open-circuit voltages of the constituent cells and the tandem device achieved an open circuit voltage \sim 1.06 V.

Finally, we summarize the PV device performance reported to date in Table 1.

5. Future challenges and directions

The prime challenge for CQD PV is further improvement in device efficiency. Materials engineering is required to improve electron and hole transport within CQD materials. Most CQD PV devices realized to date rely on materials showing mobilities of 10^{-3} cm²/V-s or lower. Preserving carrier lifetime while increasing mobility to 10^{-2} cm²/V-s and above offers an avenue to greater than 10% solar power conversion efficiencies from CQD PV.

Another interesting phenomenon called multiexciton generation (MEG), the creation of two electron-hole pairs from one high-energy photon. This phenomenon has seen much recent study in a variety of nanocrystal materials.^{76–79} MEG has been reported in a sensitized PV system composed of CQDs coupled to a bulk semiconductor.^{80,81} The exploitation of MEG to improve CQD solar cell efficiency will require (a) development of CQD material system offering MEG that is well-matched to the solar spectrum, (b) highly efficient extraction of multiple excitons,

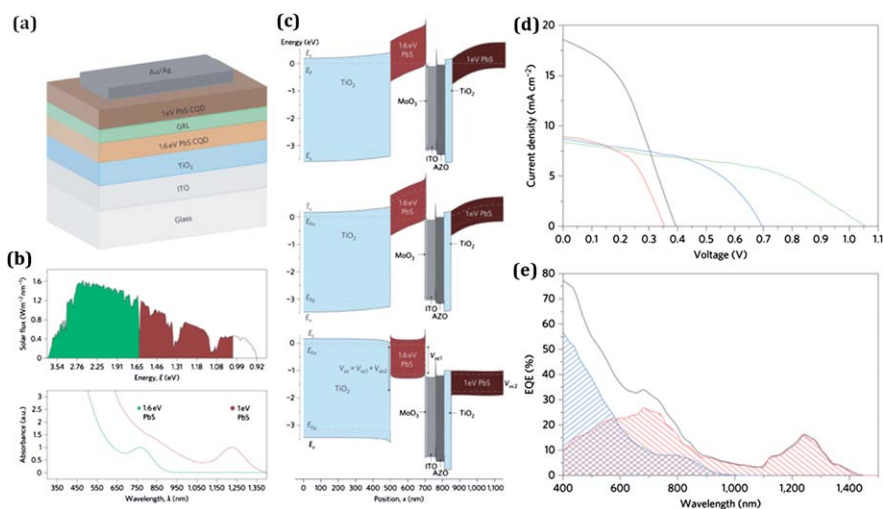


Fig. 18 (a) Tandem device architecture. (b) Spectral response from CQD tandem solar cells having quantum-confined bandgaps of 1.6 eV (green) and 1.0 eV (red) along with the absorption. (c) Spatial band diagrams for CQD tandem cells at equilibrium (top), under short-circuit (middle) and open-circuit (bottom) conditions, where E_F is the Fermi energy, E_{Fn} is the electron quasi-Fermi energy and E_{Fp} is the hole quasi-Fermi energy. (d) J-V characteristics under AM1.5 1 sun simulated illumination for the large-bandgap (blue) and small-bandgap (black) cells. J-V of the small-bandgap device when the large-bandgap CQD film is used as a filter (red). (e) EQE spectra of the large-bandgap junction with a transparent top contact (blue), the small-bandgap junction with a reflective top contact (black), and the small-bandgap junction with the large-bandgap CQD film used as filter (red).⁶⁷

Table 1 Summary of device architecture and performance of CQD based solar cells

Device Architecture	Material System	V_{oc} (V)	J_{sc} (mA/cm ²)	FF (%)	η (%)
Schottky	ITO/PbSe/Al ⁴¹	0.24	12.0	38	1.1
	ITO/PbS/Al ²⁶	0.33	12.3	44	1.8
	ITO/PbS/LiF/Al ⁶⁸	0.46	8.6	55	2.2
	ITO/PbS _x Se _{1-x} /Al ¹¹	0.45	14.8	50	3.3
	ITO/PbS/LiF/Al ⁵⁶	0.51	14	51	3.6
	ITO/PbS/LiF/Al ⁶⁹	0.57	11.3	58	3.8
	ITO/PbS/LiF/Al ⁵⁵	0.55	11.4	64	3.9
	ITO/CdTe/Al ³⁹	0.54	21.6	46	5.0
Heterojunction	ITO/TiO ₂ /(HgTe:TiO ₂)/(HgTe:P3HT)/Au ⁷⁰	0.40	2.0	50	0.4
	ITO/PbS/a-Si/Al ⁷¹	0.2	9.0	39	0.7
	ITO/ZnO/PbSe/ α -NPD/Au ⁷²	0.39	15.7	27	1.6
	ITO/PbS/C ₆₀ /LiF/Al ⁷³	0.40	10.5	52	2.2
	ITO/ZnO/PbS/Au ⁶²	0.59	8.9	56	3.0
	FTO/TiO ₂ /PbS/LiF/Ni ⁶³	0.54	10.5	59	3.5
	FTO/TiO ₂ /PbS/MoO ₃ /Ag	0.53	13.0	51	3.5
	FTO/TiO ₂ /PbS/Au ¹	0.51	16.2	58	5.1
Bulk	FTO/TiO ₂ /PbS/Au ²	0.56	17.0	61	5.7
	ITO/ZnO/PbSe/ α -NPD/Au ⁷⁴	0.42	18.6	25	2.0
	FTO/TiO ₂ /PbS/Au ⁶⁶	0.48	20.6	56	5.5
Tandem	ITO/PEDOT:PSS/PbS/ZnO/Au/PEDOT/PbS/ZnO/Al ⁷⁵	0.91	3.7	37	1.3
	ITO/TiO ₂ /PbS/GRL/PbS/Au/Ag ⁶⁷	1.06	8.3	48	4.2

including not only at a heterointerface, but just as important, throughout the entire thickness of an optically dense colloidal quantum dot film.

There exists considerable interest in employing photonic and plasmonic strategies to enhance optical absorption in CQD PV devices. Field concentration and desirable optical scattering into a film can be achieved with the aid of metallic nanostructures. Together these effects can be used to reduce the thickness of CQD film required to achieve complete absorption, thus significantly overcoming the existing absorption-extraction compromise.

There may exist opportunities to improve the density of quantum dot packing - hence the absorption per unit length - inside CQD films. This will be synergistic with efforts to enhance mobility.

Device architecture has played a major role in performance advances to date. Further advances are possible along this path. The bulk heterojunction concept can be extended to high-mobility nanowires/nanorods infiltrated with CQDs to overcome transport limitations more effectively.

CQD device stability will require further improvement. The 1000-hour result discussed above provides great encouragement for the

field on this front. Stability in the 100,000 h range is required to address the full scope of commercial opportunities. Highly durable passivation will be a key requirement to achieve this goal.

Acknowledgements

This publication is based in part on work supported by Award No. KUS-11-009-21, made by King Abdullah University of Science and Technology (KAUST), by the Ontario Research Fund Research Excellence Program, and by the Natural Sciences and Engineering Research Council (NSERC) of Canada. R. Debnath acknowledges the financial support through e8/MITACS Elevate Strategic Fellowship. We thank all group members particularly to Dr X. Wang, Dr J. Tang, Dr R. Rui, Dr S. Thon, Dr L. Brzozowski, Mr. I. J. Kramer, Mr. K. Kemp, Mrs. E. Palmiano, Mr. R. Wolowiec, Mr. D. Kopilovic and Mr. D. Jamaskosmanovic for their kind support and help during the preparation of this manuscript.

References

- A. G. Pattantyus-Abraham, I. J. Kramer, A. R. Barkhouse, X. Wang, G. Konstantatos, R. Debnath, L. Levina, I. Raabe, M. K. Nazeeruddin, M. Grätzel and E. H. Sargent, *ACS Nano*, 2010, **4**, 3374–3380.
- H. Liu, J. Tang, I. J. Kramer, R. Debnath, G. I. Koleilat, X. Wang, A. Fisher, R. Li, L. Brzozowski, L. Levina and E. H. Sargent, *Adv. Mater.*, 2011, **23**, 3832–3837.
- E. H. Sargent, *Nat. Photonics*, 2009, **3**, 325–331.
- F. Kreith and Y. Goswami, *Handbook Of Energy Efficiency And Renewable Energy*, CRC Press, Taylor and Francis Group, LLC, FL, 2007.
- J. Tang and E. H. Sargent, *Adv. Mater.*, 2011, **23**, 12–29.
- V. I. Klimov, *Nanocrystal Quantum Dots*, Springer, 2010.
- U. K. Mishra and J. Singh, *Semiconductor Device Physics and Design*, Springer, 2008.
- C. B. Murray, C. R. Kagan and M. G. Bawendi, *Annu. Rev. Mater. Sci.*, 2000, **30**, 545–610.
- M. A. Hines and G. D. Scholes, *Adv. Mater.*, 2003, **15**, 1844–1849.
- C. B. Murray, S. Sun, W. Gaschler, H. Doyle, T. A. Betley and C. R. Kagan, *IBM J. Res. Dev.*, 2001, **45**, 47–56.
- W. Ma, J. M. Luther, H. Zheng, Y. Wu and A. P. Alivisatos, *Nano Lett.*, 2009, **9**, 1699–1703.
- D. K. Smith, J. M. Luther, O. E. Semonin, A. J. Nozik and M. C. Beard, *ACS Nano*, 2011, **5**, 183–190.
- M. Sykora, A. Y. Kopysov, J. A. McGuire, R. K. Schulze, O. Tretiak, J. M. Pietryga and V. I. Klimov, *ACS Nano*, 2010, **4**, 2021–2034.
- J. Tang, X. Wang, L. Brzozowski, D. A. R. Barkhouse, R. Debnath, L. Levina and E. H. Sargent, *Adv. Mater.*, 2010, **22**, 1398–1402.
- I. Moreels, Y. Justo, B. De Geyter, K. Haustraete, J. C. Martins and Z. Hens, *ACS Nano*, 2011, **5**, 2004–2012.
- J. M. Pietryga, R. D. Schaller, D. Werder, M. H. Stewart, V. I. Klimov and J. A. Hollingsworth, *J. Am. Chem. Soc.*, 2004, **126**, 11752–11753.
- H. Zhu, N. Song and T. Lian, *J. Am. Chem. Soc.*, 2010, **132**, 15038–15045.
- G. I. Maikov, R. Vaxenburg, A. Sashchiuk and E. Lifshitz, *ACS Nano*, 2010, **4**, 6547–6556.
- S. Brovelli, R. Schaller, S. Crooker, F. García-Santamaría, Y. Chen, R. Viswanatha, J. Hollingsworth, H. Htoon and V. Klimov, *Nat. Commun.*, 2011, **2**, 280.
- D. V. Talapin, J. H. Nelson, E. V. Shevchenko, S. Aloni, B. Sadtler and A. P. Alivisatos, *Nano Lett.*, 2007, **7**, 2951–2959.
- M. G. Lupo, F. Della Sala, L. Carbone, M. Zavelani-Rossi, A. Fiore, L. Luer, D. Polli, R. Cingolani, L. Manna and G. Lanzani, *Nano Lett.*, 2008, **8**, 4582–4587.
- L. Carbone, C. Nobile, M. De Giorgi, F. Della Sala, G. Morello, P. Pompa, M. Hytch, E. Snoeck, A. Fiore and I. R. Franchini, *Nano Lett.*, 2007, **7**, 2942–2950.
- A. A. Lutich, C. Mauser, E. Da Como, J. Huang, A. Vaneski, D. V. Talapin, A. L. Rogach and J. Feldmann, *Nano Lett.*, 2010.
- D. V. Talapin, J. S. Lee, M. V. Kovalenko and E. V. Shevchenko, *Chem. Rev.*, 2010, **110**, 389–458.
- D. J. Norris, A. L. Efros and S. C. Erwin, *Science*, 2008, **319**, 1776.
- K. W. Johnston, A. G. Pattantyus-Abraham, J. P. Clifford, S. H. Myrskog, D. D. MacNeil, L. Levina and E. H. Sargent, *Appl. Phys. Lett.*, 2008, **92**, 151115.
- E. J. D. Klem, H. Shukla, S. Hinds, D. D. MacNeil, L. Levina and E. H. Sargent, *Appl. Phys. Lett.*, 2008, **92**, 212105.
- D. V. Talapin and C. B. Murray, *Science*, 2005, **310**, 86.
- S. M. Geyer, P. M. Allen, L.-Y. Chang, C. R. Wong, T. P. Osedach, N. Zhao, V. Bulovic and M. G. Bawendi, *ACS Nano*, 2010, **4**, 7373–7378.
- J. J. Urban, D. V. Talapin, E. V. Shevchenko, C. R. Kagan and C. B. Murray, *Nat. Mater.*, 2007, **6**, 115–121.
- D. K. Ko, J. J. Urban and C. B. Murray, *Nano Lett.*, 2010, **10**, 1842–1847.
- J. S. Lee, E. V. Shevchenko and D. V. Talapin, *J. Am. Chem. Soc.*, 2008, **130**, 9673–9675.
- D. Mocatta, G. Cohen, J. Schattner, O. Millo, E. Rabani and U. Banin, *Science*, 2011, **332**, 77.
- P. Reiss, M. Protière and L. Li, *Small*, 2009, **5**, 154–168.
- W. H. Evers, B. D. Nijs, L. Filion, S. Castillo, M. Dijkstra and D. Vanmaekelbergh, *Nano Lett.*, 2010, **10**, 4235–4241.
- Y. Liu, M. Gibbs, J. Puthussery, S. Gaik, R. Ihly, H. W. Hillhouse and M. Law, *Nano Lett.*, 2010, **10**, 1960–1969.
- J. J. Choi, C. R. Bealing, K. Bian, K. J. Hughes, W. Zhang, D. M. Smilgies, R. G. Hennig, J. R. Engstrom and T. Hanrath, *J. Am. Chem. Soc.*, 2011, **133**, 3131–3138.
- P. Podsiadlo, G. Krylova, B. Lee, K. Critchley, D. J. Gosztola, D. V. Talapin, P. D. Ashby and E. V. Shevchenko, *J. Am. Chem. Soc.*, 2010, **132**, 8953–8960.
- J. P. Clifford, G. Konstantatos, K. W. Johnston, S. Hoogland, L. Levina and E. H. Sargent, *Nat. Nanotechnol.*, 2008, **4**, 40–44.
- M. V. Kovalenko, M. Scheele and D. V. Talapin, *Science*, 2009, **324**, 1417.
- G. I. Koleilat, L. Levina, H. Shukla, S. H. Myrskog, S. Hinds, A. G. Pattantyus-Abraham and E. H. Sargent, *ACS Nano*, 2008, **2**, 833–840.
- J.-S. Lee, M. V. Kovalenko, J. Huang, D. S. Chung and D. V. Talapin, *Nat. Nanotechnol.*, 2011, **6**, 348–352.
- M. V. Kovalenko, M. I. Bodnarchuk, J. Zaumseil, J.-S. Lee and D. V. Talapin, *J. Am. Chem. Soc.*, 2010, **132**, 10085–10092.
- S. A. McDonald, G. Konstantatos, S. Zhang, P. W. Cyr, E. J. D. Klem, L. Levina and E. H. Sargent, *Nat. Mater.*, 2005, **4**, 138–142.
- H. Lee, H. C. Leventis, S.-J. Moon, P. Chen, S. Ito, S. A. Haque, T. Torres, F. Nüesch, T. Geiger, S. M. Zakeeruddin, M. Grätzel and M. K. Nazeeruddin, *Adv. Funct. Mater.*, 2009, **19**, 2735–2742.
- S. Giménez, *et al.*, *Nanotechnology*, 2009, **20**, 295204.
- Y. Itzhaik, O. Niitsoo, M. Page and G. Hodes, *J. Phys. Chem. C*, 2009, **113**, 4254–4256.
- A. Braga, S. Giménez, I. Concina, A. Vomiero and I. n. Mora-Sero, *J. Phys. Chem. Lett.*, 2011, **2**, 454–460.
- M. A. Hossain, J. R. Jennings, Z. Y. Koh and Q. Wang, *ACS Nano*, 2011, **5**, 3172–3181.
- S. Günes, K. P. Fritz, H. Neugebauer, N. S. Sariciftci, S. Kumar and G. D. Scholes, *Sol. Energy Mater. Sol. Cells*, 2007, **91**, 420–423.
- S.-J. Moon, Y. Itzhaik, J.-H. Yum, S. M. Zakeeruddin, G. Hodes and M. Grätzel, *J. Phys. Chem. Lett.*, 2010, **1**, 1524–1527.
- J. A. Chang, J. H. Rhee, S. H. Im, Y. H. Lee, H.-j. Kim, S. I. Seok, M. K. Nazeeruddin and M. Grätzel, *Nano Lett.*, 2010, **10**, 2609–2612.
- K. W. Johnston, A. G. Pattantyus-Abraham, J. P. Clifford, S. H. Myrskog, S. Hoogland, H. Shukla, E. J. D. Klem, L. Levina and E. H. Sargent, *Appl. Phys. Lett.*, 2008, **92**, 122111–122113.
- X. Ma, Y. Kuang, L. Bai, Z. Chang, F. Wang, X. Sun and D. G. Evans, *ACS Nano*, 2011, **5**, 3242–3249.
- K. Szendrei, W. Gomulya, M. Yarema, W. Heiss and M. A. Loi, *Appl. Phys. Lett.*, 2010, **97**, 203501–203503.
- R. Debnath, J. Tang, D. A. Barkhouse, X. Wang, A. G. Pattantyus-Abraham, L. Brzozowski, L. Levina and E. H. Sargent, *J. Am. Chem. Soc.*, 2010, **132**, 5952–5953.
- J. M. Luther, M. Law, M. C. Beard, Q. Song, M. O. Reese, R. J. Ellingson and A. J. Nozik, *Nano Lett.*, 2008, **8**, 3488–3492.

- 58 D. A. R. Barkhouse, A. G. Pattantyus-Abraham, L. Levina and E. H. Sargent, *ACS Nano*, 2008, **2**, 2356–2362.
- 59 J. D. Olson, Y. W. Rodriguez, L. D. Yang, G. B. Alers and S. A. Carter, *Appl. Phys. Lett.*, 2010, **96**, 242103–242103.
- 60 C.-Y. Liu and U. Kortshagen, *Nanoscale Res. Lett.*, 2010, **5**, 1253–1256.
- 61 A. de Kergommeaux, A. Fiore, N. Bruyant, F. Chandezon, P. Reiss, A. Pron, R. de Bettignies and J. Faure-Vincent, *Sol. Energy Mater. Sol. Cells*, 2011, **95**, 39–43.
- 62 J. M. Luther, J. Gao, M. T. Lloyd, O. E. Semonin, M. C. Beard and A. J. Nozik, *Adv. Mater.*, 2010, **22**, 3704–3707.
- 63 R. Debnath, M. T. Greiner, I. J. Kramer, A. Fischer, J. Tang, D. A. R. Barkhouse, X. Wang, L. Levina, Z. H. Lu and E. H. Sargent, *Appl. Phys. Lett.*, 2010, **97**, 023109.
- 64 D. A. R. Barkhouse, I. J. Kramer, X. Wang and E. H. Sargent, *Opt. Express*, 2010, **18**, A451–A457.
- 65 A. Pivrikas, N. S. Sariciftci, G. Juška and R. Österbacka, *Progr. Photovolt.: Res. Appl.*, 2007, **15**, 677–696.
- 66 D. A. R. Barkhouse, R. Debnath, I. J. Kramer, D. Zhitomirsky, A. G. Pattantyus-Abraham, L. Levina, L. Etgar, M. Grätzel and E. H. Sargent, *Adv. Mater.*, 2011, **23**, 3134–3138.
- 67 X. Wang, G. I. Koleilat, J. Tang, H. Liu, I. J. Kramer, R. Debnath, L. Brzozowski, D. A. R. Barkhouse, L. Levina, S. Hoogland and E. H. Sargent, *Nat. Photonics*, 2011, **5**, 480–484.
- 68 J. Tang, L. Brzozowski, D. A. R. Barkhouse, X. Wang, R. Debnath, R. Wolowiec, E. Palmiano, L. Levina, A. G. Pattantyus-Abraham, D. Jamakosmanovic and E. H. Sargent, *ACS Nano*, 2010, **4**, 869–878.
- 69 H. Fu, S.-W. Tsang, Y. Zhang, J. Ouyang, J. Lu, K. Yu and Y. Tao, *Chem. Mater.*, 2011, **23**, 1805–1810.
- 70 S. Günes, H. Neugebauer, N. S. Sariciftci, J. Roither, M. Kovalenko, G. Pillwein and W. Heiss, *Adv. Funct. Mater.*, 2006, **16**, 1095–1099.
- 71 B. Sun, A. T. Findikoglu, M. Sykora, D. J. Werder and V. I. Klimov, *Nano Lett.*, 2009, **9**, 1235–1241.
- 72 K. S. Leschkies, T. J. Beatty, M. S. Kang, D. J. Norris and E. S. Aydil, *ACS Nano*, 2009, **3**, 3638–3648.
- 73 S. W. Tsang, H. Fu, R. Wang, J. Lu, K. Yu and Y. Tao, *Appl. Phys. Lett.*, 2009, **95**, 183505.
- 74 K. S. Leschkies, A. G. Jacobs, D. J. Norris and E. S. Aydil, *Appl. Phys. Lett.*, 2009, **95**, 193103.
- 75 J. J. Choi, W. N. Wenger, R. S. Hoffman, Y.-F. Lim, J. Luria, J. Jasieniak, J. A. Marohn and T. Hanrath, *Adv. Mater.*, 2011, **23**, 3144–3148.
- 76 V. Sukhovatkin, S. Hinds, L. Brzozowski and E. H. Sargent, *Science*, 2009, **324**, 1542–1544.
- 77 J. E. Murphy, M. C. Beard, A. G. Norman, S. P. Ahrenkiel, J. C. Johnson, P. Yu, O. I. Mičić, R. J. Ellingson and A. J. Nozik, *J. Am. Chem. Soc.*, 2006, **128**, 3241–3247.
- 78 M. C. Beard, K. P. Knutsen, P. Yu, J. M. Luther, Q. Song, W. K. Metzger, R. J. Ellingson and A. J. Nozik, *Nano Lett.*, 2007, **7**, 2506–2512.
- 79 P. D. Cunningham, J. E. Boercker, E. E. Foos, M. P. Lumb, A. R. Smith, J. G. Tischler and J. S. Melinger, *Nano Lett.*, 2011, **11**, 3476–3481.
- 80 J. B. Sambur, T. Novet and B. A. Parkinson, *Science*, 2010, **330**, 63–66.
- 81 G. Nair, L.-Y. Chang, S. M. Geyer and M. G. Bawendi, *Nano Lett.*, 2011, **11**, 2145–2151.